

Geometric and Statistical Analysis of Avian Skull Morphology

Kaikwan Lau¹, Gary P. T. Choi^{1,*}

¹Department of Mathematics, The Chinese University of Hong Kong

*To whom correspondence should be addressed; E-mail: ptchoi@cuhk.edu.hk

Abstract

Understanding the growth and form of shapes is one of the most fundamental problems in biology. While many prior works have analyzed the beak shapes of Darwin's finches, other cranial features are relatively less explored. In this work, we develop geometric and statistical methods for analyzing the skull morphology of Darwin's finches and their relatives, focusing on the relationship between their skull dimensions, orbit curvature, and neurocranial geometries. Specifically, by utilizing tools in computational geometry, differential geometry, and numerical optimization, we develop efficient algorithms for quantifying various key geometric features of the skull. We then perform a statistical analysis and discover a strong correlation between skull size and orbit curvature. Based on our findings, we further establish a predictive model that can estimate the orbit curvature using easily obtainable linear skull measurements. Our results show that the predictive model is highly effective and is capable of explaining 85.48% of the variance (R-squared) in curvature with an average prediction error of only 6.35%. Altogether, our work provides a quantitative foundation for understanding the functional and evolutionary pressures that shape avian skulls, thereby offering a validated framework for future studies in comparative anatomy and evolutionary biology.

Keywords: Darwin's finches, Skull, Morphology, Geometric modelling, Statistical analysis

1 Introduction

The morphology of the avian skull offers critical insights into the evolutionary adaptations of birds to their respective ecological niches [1]. In particular, the skull is not a single functional unit but a dynamic structure where features such as the beak, cranium, and sensory organs are subject to interconnected evolutionary pressures [2]. Also, avian skull evolution is not simply a reflection of feeding ecology but is also significantly shaped by factors such as habitat density and migration [3]. Darwin's finches, a classic model for adaptive radiation,

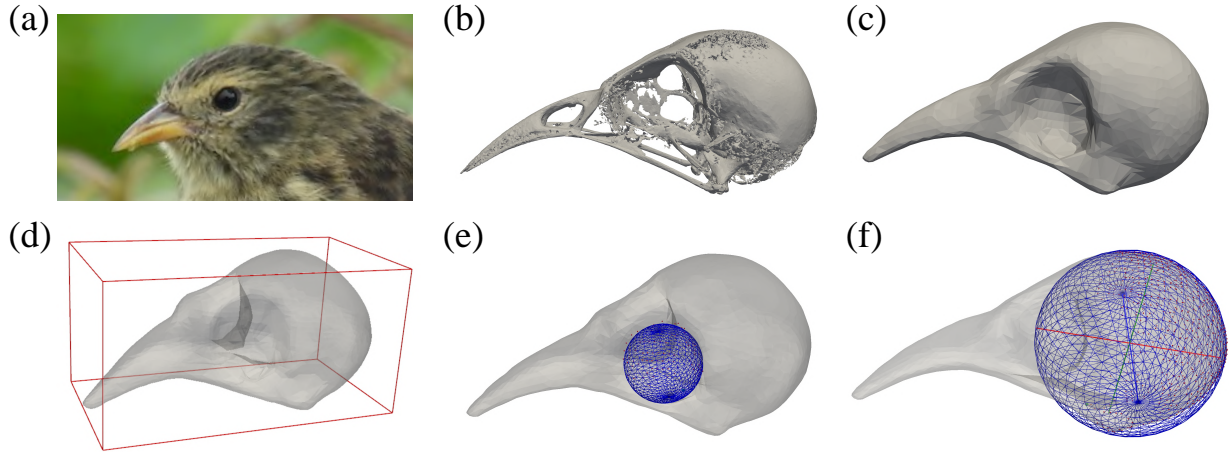


Figure 1: **An overview of the proposed skull shape quantification pipeline.** (a) An example of Darwin’s finches (*Pinaroloxias inornata*). Image credit: Howard Laidlaw (Macaulay Library at the Cornell Lab of Ornithology, Ithaca, NY) [16]. (b) A raw skull mesh of a *Pinaroloxias inornata* specimen in the dataset we considered. (c) The preprocessed skull mesh with enhanced smoothness. (d)–(f) Based on the preprocessed skull mesh, we can perform (d) bounding box calculation for quantifying the skull dimensions, (e) sphere fitting for quantifying the curvature of the orbits, and (f) ellipsoid fitting for quantifying the geometry of the neurocranium (braincase).

have been extensively studied [4–6]. In particular, most prior works have focused on the shape of the beaks of Darwin’s finches and their implications [7–10]. Besides the finch beaks, Genbrugge et al. [11] analyzed the head length, depth, and width of *Geospiza fortis*. Also, Tokita et al. [12] compared the cranial shape of Darwin’s finches and Hawaiian honeycreepers using landmark-based comparative morphometrics. However, many other cranial features of Darwin’s finches remain less studied. For other avian skulls, a few prior works have explored the relationship between the avian eye, orbit, and sclerotic ring [13], the relationship between brain shape and orbital shape [14], and the exo- and endocranial covariation [15]. Therefore, it is natural to ask whether one can extract more geometric features from the skulls of Darwin’s finches and their relatives and perform a more comprehensive analysis on the relationship between different features.

Motivated by the above works, in this paper we develop geometric and statistical methods to analyze the skull morphology of Darwin’s finches in terms of the relationship between the skull dimensions, the orbit curvature, and neurocranial geometries (see Fig. 1 for an overview). Specifically, using tools in computational geometry, differential geometry, and numerical optimization, we quantify various key geometric features from the 3D skull scans. We then perform statistical analyses to study the relationship between these features, from which we discover a strong correlation between the orbital shape and the skull dimensions. We further develop a predictive model for orbit curvature from more easily obtainable linear skull measurements, which not only reveal intriguing relationships between these geometric

quantities but also potentially aid in the reconstruction and estimation of complex geometric features of other damaged or incomplete specimens. Altogether, our work provides a deeper, quantitative understanding of the functional and evolutionary pressures that have shaped the remarkable diversity of avian skull morphology.

2 Methods

To extract various geometric features from the 3D avian skulls, we develop several methods using tools in computational geometry, differential geometry, and numerical optimization.

2.1 Dataset and Mesh Processing

In this work, we consider 100 full skull specimens of Darwin’s finches and their relatives [9, 10, 12]. The 100 specimens cover Darwin’s finches in the genera *Camarhynchus*, *Certhidea*, *Geospiza*, *Pinaroloxias*, and *Platyspiza*, and their relatives in the genera *Coereba*, *Euneornis*, *Loxigilla*, *Melopyrrha*, and *Tiaris* (see SI Section S1 for details).

We first apply the voxelization and smoothing procedure as described in [10] to remesh the original 3D scans (see Fig. 1(b) for an example) with various hole-filling and cleaning steps. As shown in Fig. 1(c), the processed mesh contains a large, contiguous component of vertices and faces with enhanced smoothness, and extraneous and disconnected artifacts are removed. This helps improve the accuracy of the subsequent geometric curvature quantification and shape fitting analysis.

Also, we enforce that all specimens are aligned within a uniform coordinate system for easier comparison and analysis. To achieve this, all raw skull meshes in the dataset are first oriented based on their principal moment directions as described in [9]. Specifically, the principal moment directions are defined as the eigen-directions of the moment tensor

$$M_{ij} = \sum_{n=1}^N (P_n \cdot P_n \delta_{ij} - P_{ni} P_{nj}), \quad (1)$$

which is calculated from all vertices $\{P_n\}_{n=1}^N$ of the 3D skull mesh, $i, j \in \{1, 2, 3\}$ correspond to the x, y, z coordinates, and δ_{ij} is the Kronecker delta. We further apply a refined rotation on the processed meshes to correct any misalignment or asymmetry caused by the mesh discretization or minor artifacts. This standardized orientation facilitates our quantification of the skull dimensions, which will be described in detail in the following section.

2.2 Linear Measurements of Skull Dimensions

From the processed meshes, we extract three key linear measurements of the skull, including the length x , width y , and height z , using a bounding box calculation approach (see Fig. 1(d)). To ensure our linear measurements were consistent and biologically meaningful, we employ the Axis-Aligned Bounding Box (AABB) approach [17], which requires pre-aligning all specimens

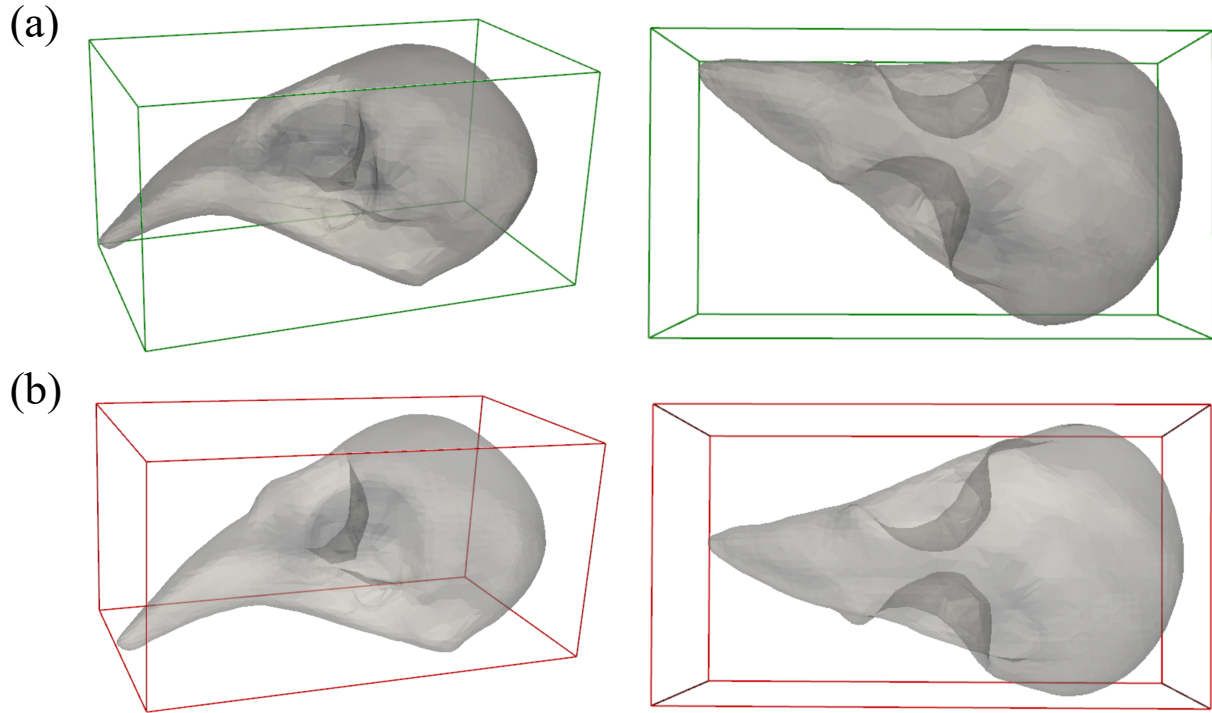


Figure 2: **Comparison between bounding box calculation methods for quantifying the skull dimensions of a *Geospiza septentrionalis* skull.** (a) The Oriented Bounding Box (OBB) result with two different views. (b) The Axis-Aligned Bounding Box (AABB) result with two different views.

to a uniform coordinate system where the x , y , and z -axes correspond to the anatomical length, width, and height, respectively. Note that one may also consider using the Oriented Bounding Box (OBB) approach [18], which allows the bounding box to rotate to better fit the object. However, we find that the OBB approach is less suitable for the geometric quantification of the skulls in our problem, as the skull may be tilted in the resulting OBB in some cases, leading to inconsistencies in the definition of length, width, and height in our analysis. For instance, as shown in Fig. 2(a), the “length” obtained from the OBB approach does not represent the dimension of the skull correctly. By contrast, the AABB approach (Fig. 2(b)) produces an axis-aligned bounding box, thereby giving more interpretable and meaningful measurements of the skull dimensions. Hence, the AABB approach is used in our study.

2.3 Automatic identification of the orbit region

Next, we utilize differential geometry for the automatic identification of the orbit region for our subsequent analysis. Specifically, note that the orbital socket is a region in the skull characterized by significant concavity. Motivated by this observation, for every vertex in the

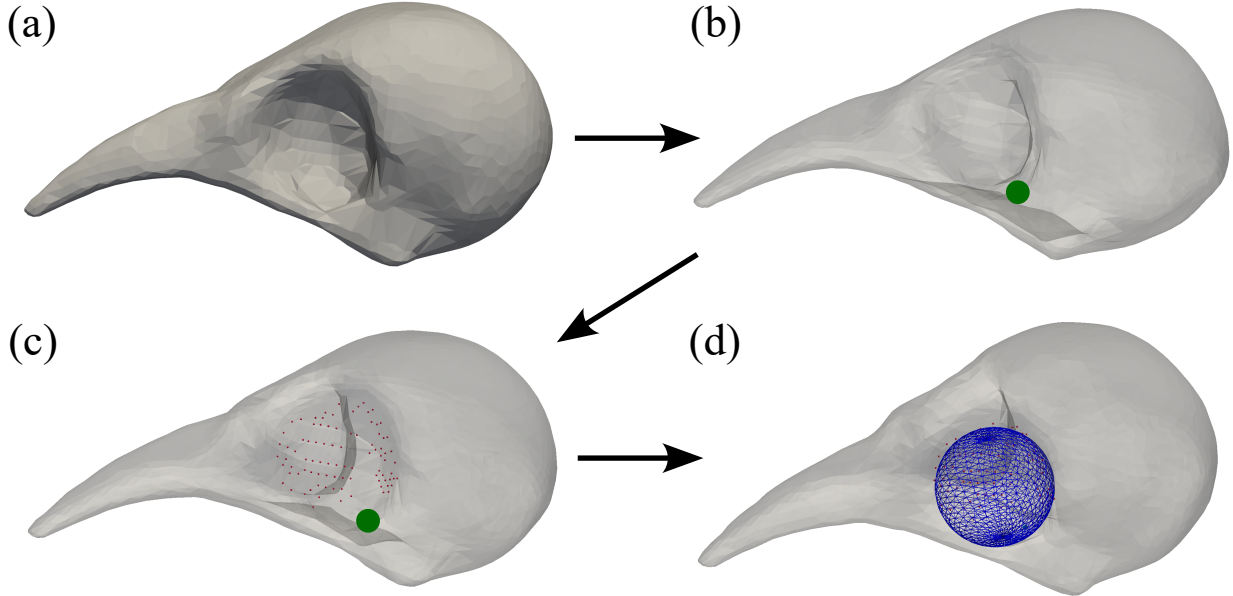


Figure 3: **An illustration of the robust and iterative sphere fitting method.** (a) A 3D skull mesh of *Pinaroloxias inornata*. (b) A seed point (green) is found to locate the orbital socket. (c) Selected points (red) are then identified via connected component identification and distance-based thresholding. (d) An optimal sphere (blue) is finally obtained via an optimization problem for approximating the curvature of the orbital socket.

skull mesh, we compute the mean curvature

$$H = \frac{1}{2}(\kappa_1 + \kappa_2), \quad (2)$$

where κ_1, κ_2 are the principal curvatures. Then, the vertices exhibiting the most pronounced negative curvature are designated as the preliminary candidate points for delineating the orbital socket. Here, note that the mean curvature was selected as our primary metric as it measures how much a surface bends at a specific point. This makes it exceptionally effective at identifying concave regions like the orbital socket, which can be thought of as a “dent” in the skull’s surface, allowing for reliable identification of our region of interest. From this pool of candidates, a singular “seed point” is established, corresponding to the vertex that possesses the absolute minimum curvature value. See Fig. 3(a)–(b) for an illustration of the above processes.

We then utilize a connected component identification approach to ensure that the analytical focus remains on a singular, coherent anatomical feature. Specifically, a contiguous cluster of points that corresponds to a single orbital socket is isolated. To achieve this, we first construct a graph from the candidate points. Then, the connected component containing the above-mentioned seed point is extracted. However, it is noteworthy that the mean curvature computation relies on the discretization of the mesh and may be affected by minor variations of the vertices locally. To further obtain a unified quantity representing the orbit curvature,

in the subsequent section we develop a sphere fitting algorithm based on the points extracted from the connected component.

2.4 Robust and Iterative Sphere Fitting

To quantify the geometry of the orbital socket, we develop a robust and iterative sphere fitting algorithm (Fig. 1(e)). Specifically, the fitting procedure is formulated as an optimization problem that seeks to minimize a loss function, defined as the sum of squared Euclidean distances from each point to the surface of a candidate sphere. To enhance the robustness and accuracy of the fit, an iterative scheme is developed. Within each iteration, a sphere is fitted to the current point set, followed by the identification and removal of outlier points, which are defined as points whose distance from the sphere’s surface exceeds a predetermined threshold based on the standard deviation of the distances (see Fig. 3(c)). This process of iterative outlier removal ensures that the final sphere parameters provide a more precise and representative geometric model of the feature. The mathematical formulation for this process is as follows.

Let $P = \{p_1, p_2, \dots, p_n\}$, where each point $p_i = (x_i, y_i, z_i)$ is a vector in \mathbb{R}^3 . A sphere is defined by its center $C = (c_x, c_y, c_z)$ and its radius r . The objective is to find the parameters (C, r) that best fit the points in P (see Fig. 3(d)). The distance of a point p_i from the center C is given by the Euclidean norm:

$$d_i = \|p_i - C\| = \sqrt{(x_i - c_x)^2 + (y_i - c_y)^2 + (z_i - c_z)^2}. \quad (3)$$

The error for a single point, e_i , is then defined as the absolute difference between its distance from the center and the sphere’s radius:

$$e_i = |d_i - r| = |\|p_i - C\| - r|. \quad (4)$$

In other words, e_i represents the shortest distance from the point to the surface of the sphere.

Now, since the objective is to find the sphere parameters that best fit the points in P , we define the loss function $\mathcal{L}(C, r)$ as the sum of the squared errors for all points in the point set P :

$$\mathcal{L}(C, r) = \sum_{i=1}^n e_i^2 = \sum_{i=1}^n (\|p_i - C\| - r)^2. \quad (5)$$

Then, the optimization problem is to find the parameters that minimize this function:

$$(\hat{C}, \hat{r}) = \underset{C \in \mathbb{R}^3, r \in \mathbb{R}^+}{\operatorname{argmin}} \mathcal{L}(C, r). \quad (6)$$

To solve the above-mentioned optimization problem of fitting a sphere to the data points, we use the Limited-memory Broyden–Fletcher–Goldfarb–Shann (L-BFGS-B) algorithm [19] as it is a quasi-Newton method highly adept at solving non-linear optimization problems. This approach is computationally efficient and, critically, allows for the enforcement of bound constraints, which is essential for ensuring a physically realistic solution by requiring the

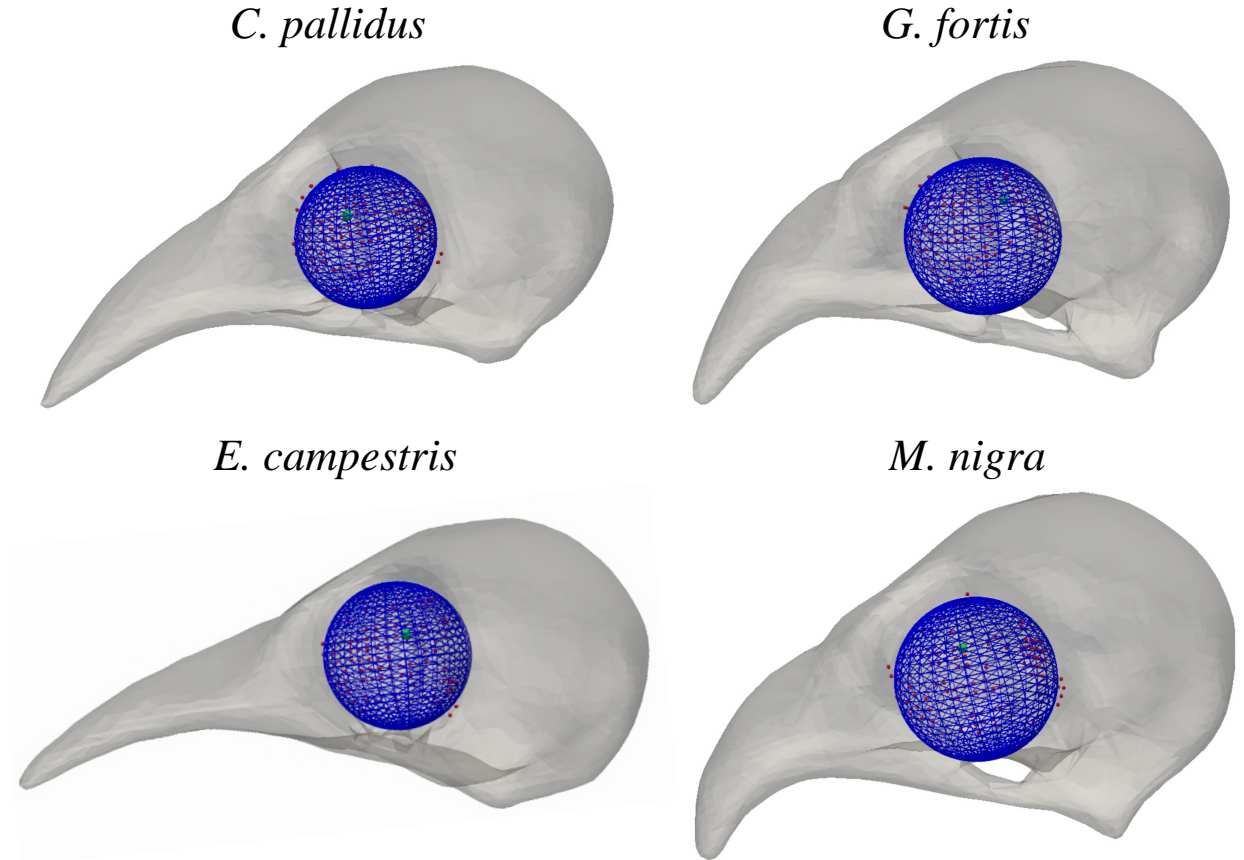


Figure 4: **Four examples of the sphere fitting results for orbit curvature quantification.** In each example, the seed point is highlighted in green, and the identified points for the fitting are highlighted in red. The optimal sphere is displayed in blue. Note that the figures are not displayed to scale.

sphere’s radius to be a positive value. We also enforce that the sphere center and radius lie within a specific range throughout the optimization process to ensure the validity of the fitting result. Specifically, we only consider the middle 40% of the skull mesh as the “Region of Interest” (ROI) in the optimization. Finally, the orbit curvature is computed by $1/\hat{r}$, where \hat{r} is the sphere radius. In Fig. 4, we show several examples of the sphere fitting results, from which we can see that the method is capable of quantifying the orbit curvature for different skull specimens. More examples are provided in SI Section S1.

2.5 Extension to Ellipsoid Fitting of Neurocranium

By extending the above-mentioned sphere fitting algorithm, we can achieve an ellipsoid fitting of the neurocranium of the skull and quantify the shape of the braincase using the ellipsoidal semi-axis lengths a, b, c (see Fig. 5 for an illustration).

Specifically, to ensure that the ellipsoidal fitting analysis is performed on the neurocranium

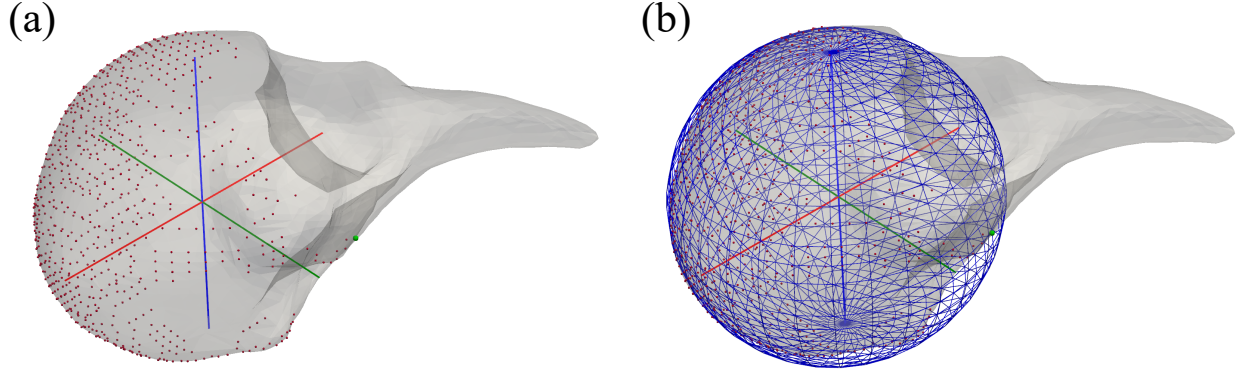


Figure 5: **An illustration of the ellipsoid fitting algorithm for a *Pinaroloxias inornata* skull.** (a) The input skull mesh with the seed point (green dot), selected points (red dots), and the computed axis a (red line), b (green line), and c (blue line). (b) The best-fit ellipsoid obtained by the proposed algorithm.

of the skull, we first calculate a cutoff coordinate for isolating the posterior region of the 3D skull mesh based on a prescribed threshold. We then select all vertices in the mesh that are beyond this cutoff, effectively isolating the rearmost 40% of the skull. This area becomes the ROI for our neurocranial shape quantification. Within this ROI, we search for the single most outwardly curved (convex) point and designate it as the “seed point”. This provides a reliable starting anchor on the roundest part of the neurocranium. We further refine the selection to get the best possible set of points. Specifically, a large group of the most convex points within the ROI is then identified based on a prescribed parameter. To avoid using scattered points, we adopt a similar strategy as in the previously described orbit analysis and perform a connected component identification procedure. Starting from the seed point, we find all the points from the “curved” cloud that are connected to it. This results in a single, coherent patch of points on the surface of the neurocranium, which is an ideal input for the ellipsoid fitting algorithm.

Similar to the sphere fitting algorithm for the orbit, we take the clean patch of points and find the best possible axis-aligned ellipsoid to fit them. To achieve this, we use an optimizer from the `scipy` library in Python and perform an iterative fitting process to improve accuracy. The method repeatedly guesses the center and axis lengths, measures how far the points are from the surface of its guessed ellipsoid (the “error”), and then makes a new, improved guess to reduce the error. This process continues until the method finds the parameters within a prescribed range that give the minimum possible error, representing the best fit. Moreover, after the initial fit, we identify any points that lie too far from the fitted surface (“outliers”). We then remove these outliers and run the entire optimization process again on the cleaner set of points. This makes the final result more accurate and less sensitive to noise. In Fig. 6, we show several examples of the ellipsoid fitting results, from which it can be observed that the algorithm handles different neurocranial geometries very well. More examples are provided in SI Section S1.

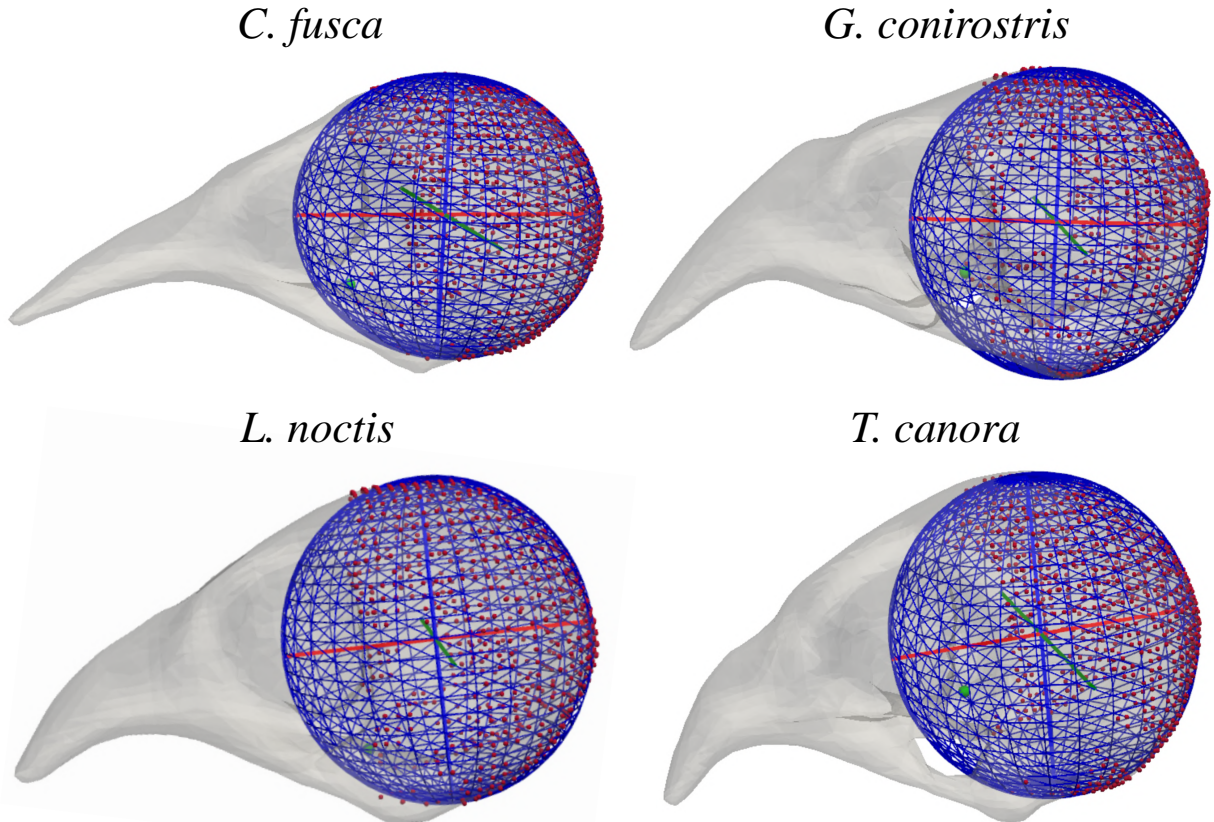


Figure 6: **Four examples of the ellipsoid fitting results for neurocranial geometry quantification.** In each example, the seed point is highlighted in green, and the identified points for the fitting are highlighted in red. The optimal ellipsoid is displayed in blue. Note that the figures are not displayed to scale.

3 Results and Analyses

3.1 Correlation between Skull Dimensions and Orbit Curvature

After applying the proposed approaches for extracting the skull dimension and geometric curvature parameters, we perform a statistical analysis on the quantities. In particular, our analysis reveals a strong correlation between the dimensions of the skull and the curvature of the orbit (see Fig. 7). For both Darwin’s finches and their relatives, a high Spearman correlation is observed between the sphere radius (inversely related to the orbit curvature) and the skull’s length, width, and height. Specifically, for Darwin’s finches, the Spearman correlation coefficients between sphere radius and length x , width y , and height z are 0.740, 0.802, and 0.774, respectively. For the relatives of Darwin’s finches, these correlations are even stronger: 0.708, 0.843, and 0.893. This indicates that larger skulls tend to have larger orbit radii, and therefore, lower curvature. The Pearson correlation analysis confirms this inverse relationship, showing negative correlations between curvature and the skull dimensions. If

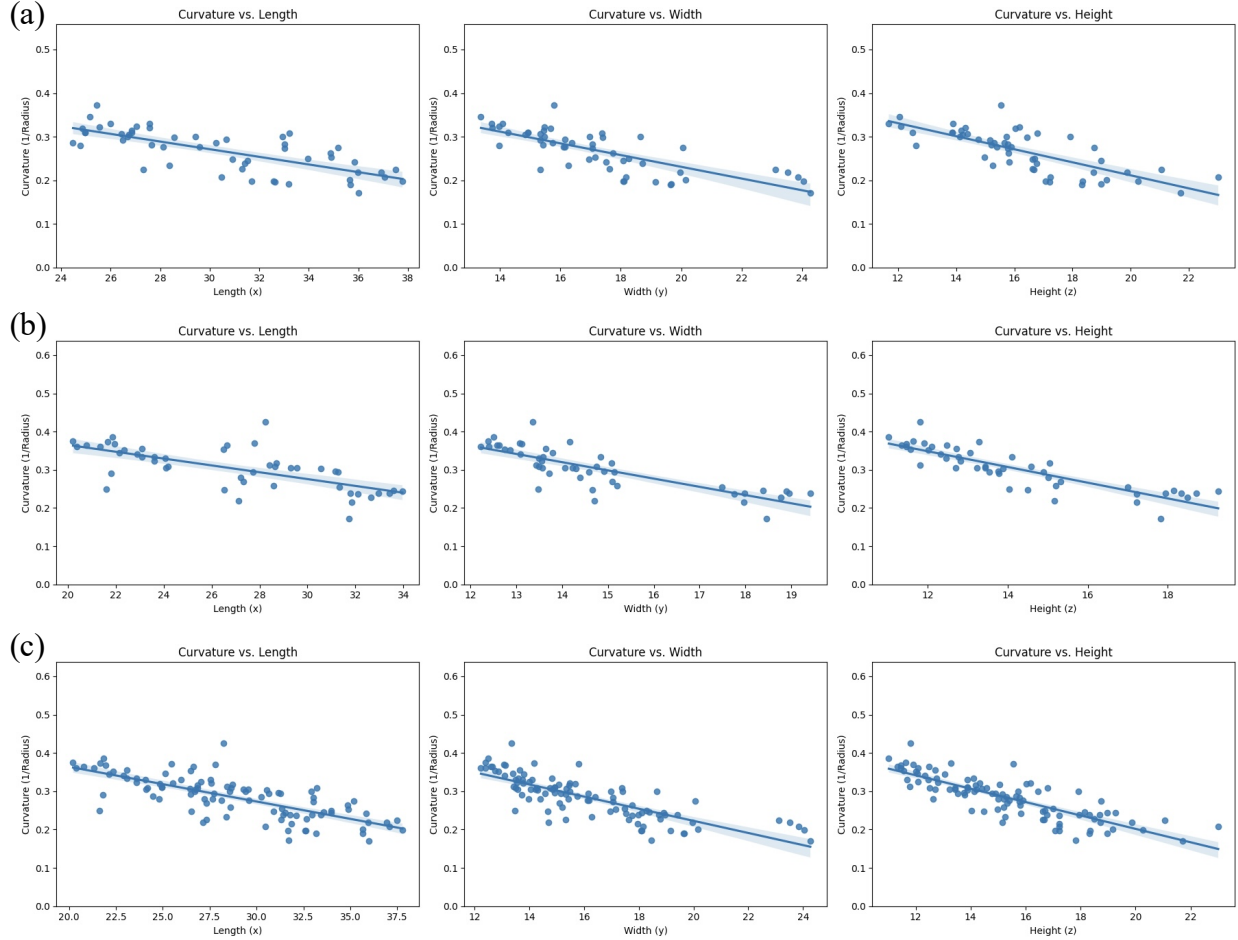


Figure 7: **Correlation between different geometric parameters of the skulls of Darwin’s finches and their relatives.** Each plot shows the correlation between the orbit curvature against an object dimension parameter (length/width/height) for (a) Darwin’s finches, (b) their relatives, and (c) both groups combined. The blue line represents the regression line in each plot, and the shaded region around each regression line represents the confidence interval for the linear approximation.

we consider all Darwin’s finches and their relatives together, the correlation coefficients are 0.758, 0.832, and 0.844. It is noteworthy that these findings align with established principles of biological scaling, or allometry, where the relative size of anatomical features changes with overall body size [20].

Also, note that the shaded region around each regression line in Fig. 7 represents the confidence interval for the linear approximation. For the main cluster of data points (curvature between 0.2 and 0.4), this interval is relatively narrow, indicating that the linear model is a reasonable approximation for describing the central tendency of the data. More detailed statistical results are provided in SI Section S2.

3.2 Curvature Modeling and Prediction

As shown in the analysis above, there is a strong linear relationship between the curvature of the orbit and the dimensions of the skull. To investigate the relationship between skull dimensions and orbit curvature further, we develop a multiple linear regression model [21]. The dataset, consisting of 100 skull meshes, is divided into a training set (50 meshes) and a testing set (50 meshes). The model predicts the orbit curvature based on the skull’s length x , width y , and height z . The resulting best-fit equation is:

$$\text{Curvature} = 0.5653 - 0.0013x - 0.0004y - 0.0153z. \quad (7)$$

In Fig. 8, we show the data points with the actual (measured) orbit curvature and the predicted curvature values obtained by the above best-fit model. It can be observed that the curvature distributions are highly consistent, providing strong evidence for the relationships between the curvature and skull dimensions.

For a more quantitative analysis, we further evaluate the performance of the model by comparing the predicted curvature values with the actual curvature values from the testing set. The relative error is calculated using the following formula:

$$\text{Relative Error} = \frac{|\text{Actual curvature} - \text{Predict curvature}|}{\text{Actual curvature}}. \quad (8)$$

The multiple linear regression model we developed demonstrates a high degree of effectiveness. Specifically, the model achieves an adjusted R-squared value of 0.8548, indicating that 85.48% of the variance in orbit curvature can be explained by the skull’s primary dimensions. A potential anatomical basis for this strong correlation is the highly integrated nature of the modern avian skull. As detailed by Plateau and Foth [22], the evolutionary trend of bone fusion and integration created a structurally unified avian skull. This unity imposes strict rules on how the skull can grow and change shape, resulting in the strong, predictable allometric correlations between different features that we were able to model successfully. Also, the F-statistic probability is extremely low (6.86×10^{-8}), confirming that the model’s predictive power is not due to random chance [23]. The model’s accuracy is further validated by comparing its predictions to the actual curvature values of the 50 test samples. The average relative error for all 50 test samples is a low 6.53%, with a minimum error of 0.064% and a maximum of 27.93%. A significant majority of the predictions (39/50, i.e., 78%) have a relative error below 10%, over half of the predictions (26/50, i.e., 52%) have a relative error below 5%, and a substantial portion (11/50, i.e., 22%) further exhibit a relative error below 1%. This demonstrates the model’s robustness and its potential for use in sensitive scientific analyses.

From a biological perspective, Eq. (7) shows that generally a higher dimension size of the head results in a lower curvature. Eventually, by taking the inverse, we will have a higher orbit. This result follows the usual developmental process of the skull in one of Darwin’s finches by illustrating that the orbit’s development is intrinsically linked to the growth of the entire skull, meaning a larger overall skull results from a growth process that also produces larger orbits [24]. Besides, from a computational perspective, the regression model demonstrates the

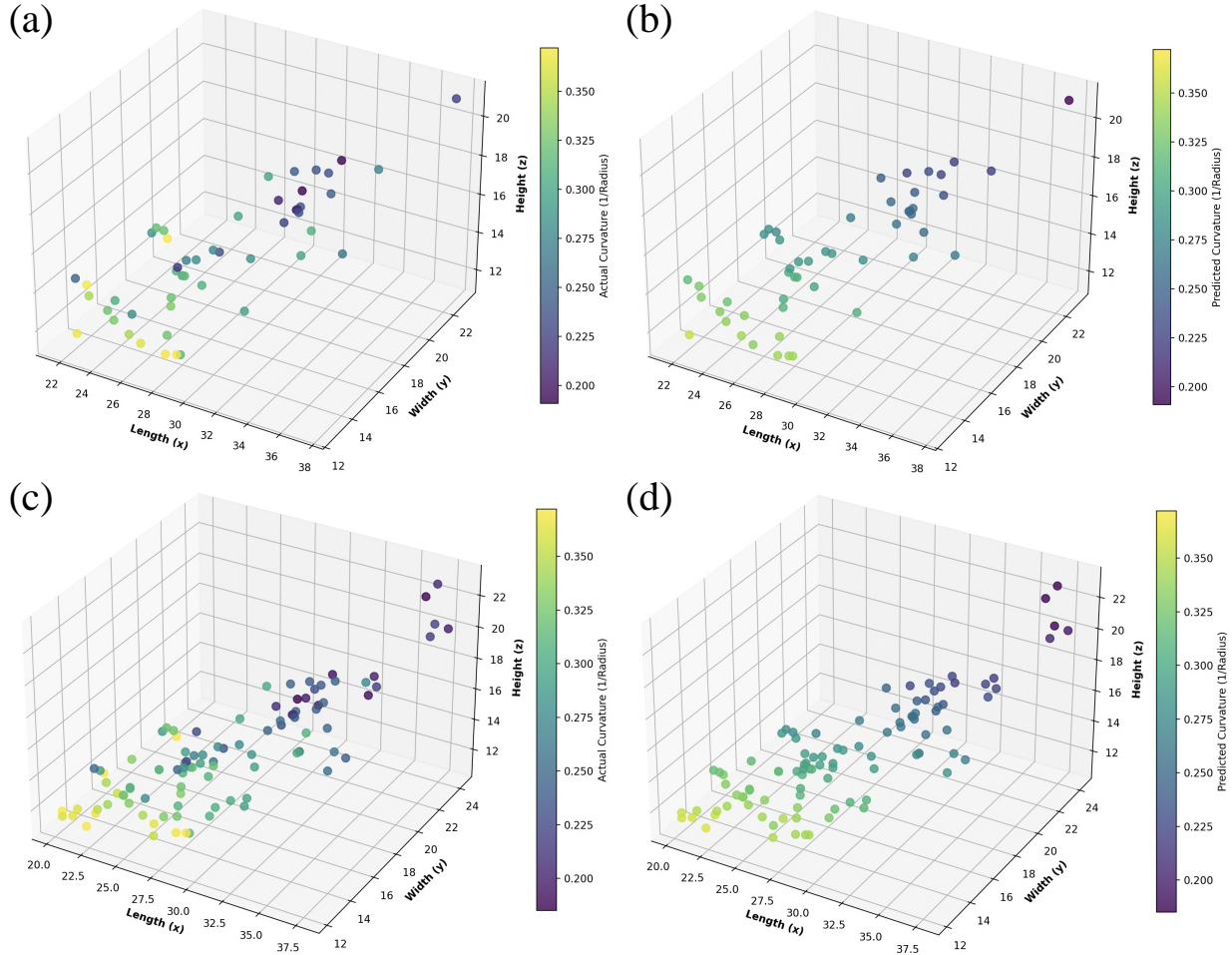


Figure 8: **Orbit curvature estimation from skull dimensions via our proposed model.** (a) The 50 training samples with the coordinates of each point representing the skull dimensions (x, y, z) and the colors representing the actual (measured) orbit curvature. (b) The data points color-coded with the predicted curvature obtained using the best-fit multiple linear regression model in Eq. (7). It can be observed that the curvature distributions in the two plots are highly consistent. (c) The actual (measured) orbit curvature for all 100 specimens. (d) The predicted curvature for all 100 specimens obtained using the model.

possibility of predicting complex geometric features from more easily obtainable linear skull measurements. This not only largely reduces the computational costs for shape quantification but also provides a promising direction for reconstructing or estimating complex features from damaged or incomplete specimens for further computational analyses.

3.3 Correlation between Neurocranial Shapes and Other Features

Also, using the proposed ellipsoid fitting algorithm for quantifying the neurocranium, we analyze the relationship between the ellipsoidal semi-axis lengths and other geometric features of the skull.

In particular, a strong negative correlation is consistently observed between the lengths of the ellipsoid semi-axes (a , b , and c) and the orbit curvature. This indicates that as the overall size of the neurocranium increases (as modeled by the ellipsoid dimensions), the curvature of the orbit becomes quantitatively less curved. This inverse relationship is robust, evident in both Pearson and Spearman analyses (see SI Section S3 for the detailed statistical results). Therefore, the algorithm not only quantifies size and shape independently but also captures the intrinsic geometric link between them, providing a quantitative framework for understanding how the scale of a cranial structure relates to its local topography. Moreover, in analyzing skull morphology, the semi-axes are more biologically informative than standard linear measurements because they directly represent the dimensions of the neurocranium. We find that a larger principal semi-axis, corresponding to a larger neurocranium, results in a smaller orbit curvature. This matches the findings that the developments of the braincase and large orbits are not separate but are two facets of the same core retaining juvenile traits process [12, 25].

4 Discussion

In this work, we have developed a suite of mathematical tools for analyzing avian skull morphology using geometric computing and statistical modelling. In particular, using our proposed approaches, we have uncovered the intricate relationships between several key geometric measurements in the skulls of Darwin’s finches and their relatives. We have further developed and validated a predictive model for orbit curvature based on skull dimensions, which shows a high degree of accuracy and reliability. These findings contribute to a deeper understanding of the biomechanics and evolutionary adaptations of avian skulls.

More broadly, our study demonstrates the possibility of estimating and predicting complex geometric features in avian skulls from easily obtainable linear dimension measurements, which could be utilized for streamlining the process of various skull modelling and morphological analysis tasks. It could also potentially aid in the reconstruction of damaged or incomplete specimens in which direct measurements of certain complex geometric features are impossible. Ultimately, the methodologies and results presented in this paper provide a solid foundation for future exploration in comparative anatomy and functional morphology, opening new avenues for quantitative analysis in the field of ornithology and beyond.

References

- [1] W. J. Bock, “The avian skull,” in *Avian Biology* (D. S. Farner and J. R. King, eds.), vol. 4, pp. 1–182, Academic Press, Cambridge, MA, USA, 1974.

- [2] R. L. Zusi, “Patterns of diversification in the avian skull,” in *The Skull* (J. Hanken and B. K. Hall, eds.), vol. 3, pp. 391–437, University of Chicago Press, Chicago, IL, USA, 1993.
- [3] E. S. Hunt, R. N. Felice, J. A. Tobias, and A. Goswami, “Ecological and life-history drivers of avian skull evolution,” *Evolution*, vol. 77, no. 7, pp. 1720–1729, 2023.
- [4] P. R. Grant and B. R. Grant, *40 years of evolution: Darwin’s finches on Daphne Major Island*. Princeton University Press, Princeton, NJ, USA, 2014.
- [5] H. L. Farrington, L. P. Lawson, C. M. Clark, and K. Petren, “The evolutionary history of Darwin’s finches: speciation, gene flow, and introgression in a fragmented landscape,” *Evolution*, vol. 68, no. 10, pp. 2932–2944, 2014.
- [6] G. Navalón, J. Marugán-Lobón, J. A. Bright, C. R. Cooney, and E. J. Rayfield, “The consequences of craniofacial integration for the adaptive radiations of Darwin’s finches and Hawaiian honeycreepers,” *Nature Ecology & Evolution*, vol. 4, no. 2, pp. 270–278, 2020.
- [7] A. Herrel, J. Podos, S. K. Huber, and A. P. Hendry, “Bite performance and morphology in a population of Darwin’s finches: implications for the evolution of beak shape,” *Functional Ecology*, vol. 19, no. 1, pp. 43–48, 2005.
- [8] P. R. Grant and B. R. Grant, “Evolution of character displacement in Darwin’s finches,” *Science*, vol. 313, no. 5784, pp. 224–226, 2006.
- [9] S. Al-Mosleh, G. P. T. Choi, A. Abzhanov, and L. Mahadevan, “Geometry and dynamics link form, function, and evolution of finch beaks,” *Proceedings of the National Academy of Sciences*, vol. 118, no. 46, p. e2105957118, 2021.
- [10] S. Mosleh, G. P. T. Choi, G. M. Musser, H. F. James, A. Abzhanov, and L. Mahadevan, “Beak morphometry and morphogenesis across avian radiations,” *Proceedings of the Royal Society B*, vol. 290, no. 2007, p. 20230420, 2023.
- [11] A. Genbrugge, A. Herrel, M. Boone, L. Van Hoorebeke, J. Podos, J. Dirckx, P. Aerts, and A. Dominique, “The head of the finch: the anatomy of the feeding system in two species of finches (*Geospiza fortis* and *Padda oryzivora*),” *Journal of Anatomy*, vol. 219, no. 6, pp. 676–695, 2011.
- [12] M. Tokita, W. Yano, H. F. James, and A. Abzhanov, “Cranial shape evolution in adaptive radiations of birds: comparative morphometrics of Darwin’s finches and Hawaiian honeycreepers,” *Philosophical Transactions of the Royal Society B: Biological Sciences*, vol. 372, no. 1713, p. 20150481, 2017.
- [13] M. I. Hall, “The anatomical relationships between the avian eye, orbit and sclerotic ring: implications for inferring activity patterns in extinct birds,” *Journal of Anatomy*, vol. 212, no. 6, pp. 781–794, 2008.

- [14] S. Kawabe, T. Shimokawa, H. Miki, S. Matsuda, and H. Endo, “Variation in avian brain shape: relationship with size and orbital shape,” *Journal of Anatomy*, vol. 223, no. 5, pp. 495–508, 2013.
- [15] J. Marugán-Lobón and Á. D. Buscalioni, “Avian skull morphological evolution: exploring exo-and endocranial covariation with two-block partial least squares,” *Zoology*, vol. 109, no. 3, pp. 217–230, 2006.
- [16] H. Laidlaw, “ML300431881 Cocos Finch *Pinaroloxias inornata*, Macaulay Library, Cornell Lab of Ornithology, Ithaca, NY, USA.” <https://macaulaylibrary.org/asset/300431881>, 2021.
- [17] G. van den Bergen, “Efficient collision detection of complex deformable models using AABB trees,” *Journal of Graphics Tools*, vol. 2, no. 4, pp. 1–13, 1997.
- [18] S. Gottschalk, M. C. Lin, and D. Manocha, “OBBTree: A hierarchical structure for rapid interference detection,” in *Proceedings of the 23rd Annual Conference on Computer Graphics and Interactive Techniques*, pp. 171–180, 1996.
- [19] R. H. Byrd, P. Lu, J. Nocedal, and C. Zhu, “A limited memory algorithm for bound constrained optimization,” *SIAM Journal on Scientific Computing*, vol. 16, no. 5, pp. 1190–1208, 1995.
- [20] K. Schmidt-Nielsen, *Scaling: Why is animal size so important?* Cambridge University Press, Cambridge, UK, 1984.
- [21] N. R. Draper and H. Smith, *Applied regression analysis*. John Wiley & Sons, New York City, NY, USA, 1998.
- [22] O. Plateau and C. Foth, “Birds have peramorphic skulls, too: anatomical network analyses reveal oppositional heterochronies in avian skull evolution,” *Communications Biology*, vol. 3, no. 1, p. 195, 2020.
- [23] G. James, D. Witten, T. Hastie, and R. Tibshirani, *An introduction to statistical learning: with applications in R*, vol. 103. Springer New York, NY, 2013.
- [24] A. Genbrugge, A.-S. Heyde, D. Adriaens, M. Boone, L. Van Hoorebeke, J. Dirckx, P. Aerts, J. Podos, and A. Herrel, “Ontogeny of the cranial skeleton in a Darwin’s finch (*Geospiza fortis*),” *Journal of Anatomy*, vol. 219, no. 2, pp. 115–131, 2011.
- [25] B.-A. S. Bhullar, J. Marugán-Lobón, F. Racimo, G. S. Bever, T. B. Rowe, M. A. Norell, and A. Abzhanov, “Birds have paedomorphic dinosaur skulls,” *Nature*, vol. 487, no. 7406, pp. 223–226, 2012.

Supplementary Information

S1 Skull Dataset and Geometric Quantification

In this work, we considered 100 specimens of Darwin’s finches and their relatives from [9,10,12] for our experiments. Table S1 and Table S2 list the genus and species of each of the 100 specimens.

As described in the main text, we first remeshed the 3D scans and enhanced the mesh quality for subsequent analysis. Note that while the relevant voxelization and smoothing procedures were also performed in [9,10], these prior studies focused on the analysis of the beak shapes, and hence their remeshing setups only preserved the beak shape well while oversimplifying many other features of the skulls, such as the orbit (see Fig. S1, left). This makes the remeshing results from these prior studies not directly applicable to our analysis in this work. Therefore, we re-ran the mesh processing procedure on the raw 3D scans with a refined remeshing setup to improve the preservation of the skull features (see Fig. S1, right). The new remeshed surfaces were then used for the subsequent geometric and statistical analysis.

Also, in the main text, we described our proposed sphere and ellipsoid fitting algorithms for extracting geometric measurements from skull meshes. In Fig. S2, we show additional examples of the sphere fitting results for orbit curvature quantification. In Fig. S3, we show additional examples of the ellipsoid fitting results for the neurocranial geometry quantification. From these results, it can be observed that our proposed algorithms effectively capture the geometric features of a large variety of skull meshes.

S2 Statistical Analysis on Orbit Geometries

As part of our statistical shape analysis, we studied the correlation between the skull dimensions (width x , length y , height z) and orbit curvature of Darwin’s finches (DF), their relatives, and all of them. Below, we provide more detailed results of the statistical analysis.

In Table S3, we first calculate the Pearson correlation (Linear) between skull dimensions and the radius of the best-fit spheres to the orbit (i.e., $1/(\text{orbit curvature})$). Also, Table S4 records Spearman correlation (Monotonic) between skull dimensions and $1/(\text{orbit curvature})$. From both tables, we can see a strong positive correlation between the skull dimensions and the fitted sphere radius.

In Table S5 and Table S6, we further compute the Pearson correlation and Spearman correlation between the skull dimensions and the orbit curvature directly. As expected, we observe a strong negative correlation between skull dimensions and orbit curvature.

S3 Statistical Analysis on Neurocranial Geometries

We also studied the correlation between the geometry of the neurocranium of the skull and the other geometric quantities of Darwin's finches (DF), their relatives, and all of them, using the ellipsoid fitting algorithm as described in the main text.

In particular, we calculated the Pearson and Spearman correlations between the lengths of the ellipsoid semi-axes (a , b , c) and the orbit curvature of Darwin's finches, their relatives, and all of them. Table S7 and Table S8 record the results for Darwin's finches. Table S9 and Table S10 record the results for the relatives of Darwin's finches. Table S11 and Table S12 record the results for all of them.

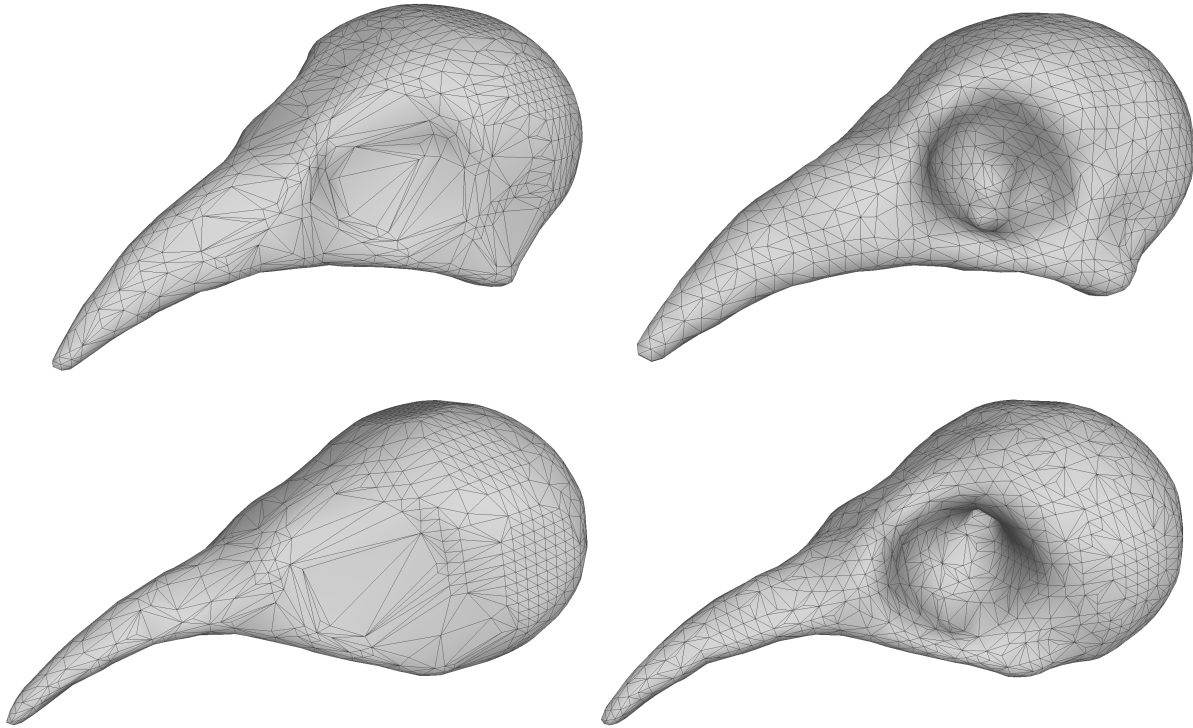


Figure S1: Remeshing of the skull specimens in the dataset. The left column shows the remeshing results by the prior studies [9, 10], the right column shows the new remeshing results done in this work. Top row: A specimen of Darwin's finches (*Camarhynchus pallidus*). Bottom: A specimen of the relatives of Darwin's finches (*Coereba flaveola*).

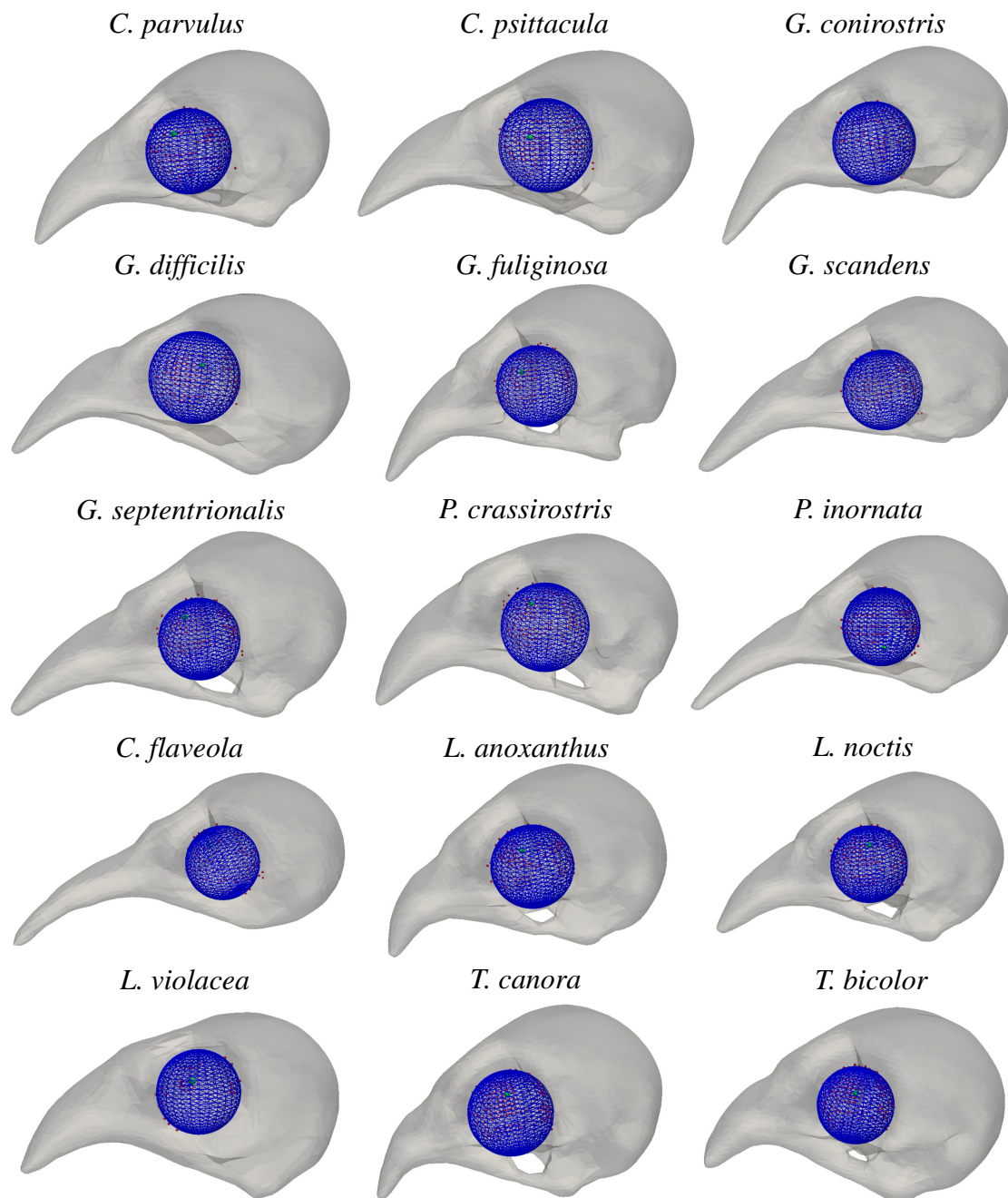


Figure S2: More examples of the sphere fitting results for orbit curvature quantification achieved by our proposed algorithm. The first three rows show examples of Darwin’s finches. The last two rows show examples of the relatives of Darwin’s finches. In each example, the seed point is highlighted in green, and the identified points for the fitting are highlighted in red. The optimal sphere is displayed in blue. The figures are not displayed to scale.

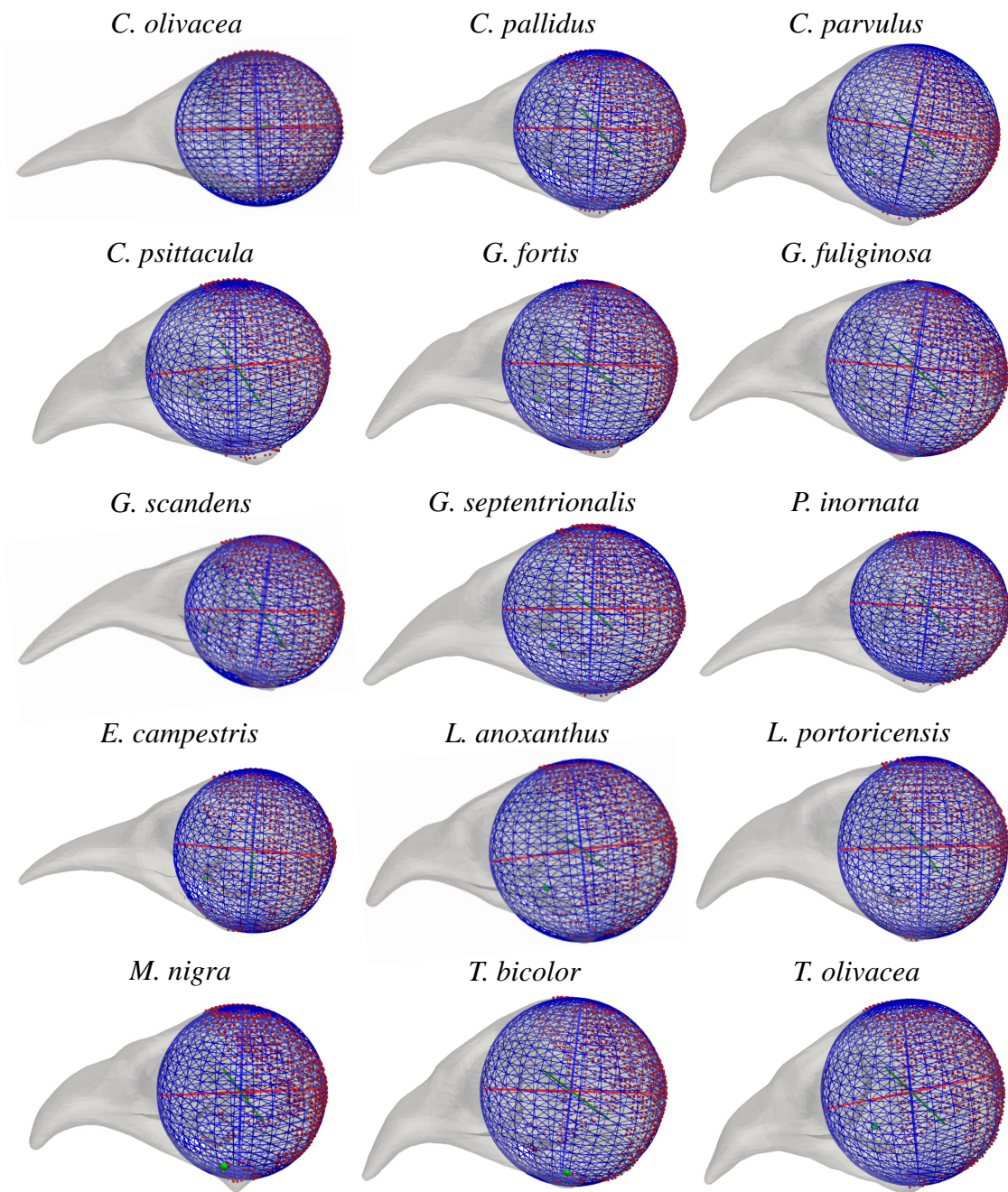


Figure S3: More examples of the ellipsoid fitting results for neurocranial geometry quantification achieved by our proposed algorithm. The first three rows show examples of Darwin's finches. The last two rows show examples of the relatives of Darwin's finches. In each example, the seed point is highlighted in green, and the identified points for the fitting are highlighted in red. The optimal ellipsoid is displayed in blue. The figures are not displayed to scale.

Specimen ID	Genus	Species
1	<i>Camarhynchus</i> (Tree Finch)	<i>pallidus</i>
2	<i>Camarhynchus</i> (Tree Finch)	<i>pallidus</i>
3	<i>Camarhynchus</i> (Tree Finch)	<i>pallidus</i>
4	<i>Camarhynchus</i> (Tree Finch)	<i>pallidus</i>
5	<i>Camarhynchus</i> (Tree Finch)	<i>parvulus</i>
6	<i>Camarhynchus</i> (Tree Finch)	<i>parvulus</i>
7	<i>Camarhynchus</i> (Tree Finch)	<i>parvulus</i>
8	<i>Camarhynchus</i> (Tree Finch)	<i>parvulus</i>
9	<i>Camarhynchus</i> (Tree Finch)	<i>parvulus</i>
10	<i>Camarhynchus</i> (Tree Finch)	<i>psittacula</i>
11	<i>Camarhynchus</i> (Tree Finch)	<i>psittacula</i>
12	<i>Camarhynchus</i> (Tree Finch)	<i>psittacula</i>
13	<i>Camarhynchus</i> (Tree Finch)	<i>psittacula</i>
14	<i>Certhidea</i> (Warbler Finch)	<i>fusca</i>
15	<i>Certhidea</i> (Warbler Finch)	<i>fusca</i>
16	<i>Certhidea</i> (Warbler Finch)	<i>olivacea</i>
17	<i>Certhidea</i> (Warbler Finch)	<i>olivacea</i>
18	<i>Certhidea</i> (Warbler Finch)	<i>olivacea</i>
19	<i>Geospiza</i> (Ground Finch)	<i>conirostris</i>
20	<i>Geospiza</i> (Ground Finch)	<i>conirostris</i>
21	<i>Geospiza</i> (Ground Finch)	<i>conirostris</i>
22	<i>Geospiza</i> (Ground Finch)	<i>conirostris</i>
23	<i>Geospiza</i> (Ground Finch)	<i>conirostris</i>
24	<i>Geospiza</i> (Ground Finch)	<i>conirostris</i>
25	<i>Geospiza</i> (Ground Finch)	<i>conirostris</i>
26	<i>Geospiza</i> (Ground Finch)	<i>difficilis</i>
27	<i>Geospiza</i> (Ground Finch)	<i>difficilis</i>
28	<i>Geospiza</i> (Ground Finch)	<i>fortis</i>
29	<i>Geospiza</i> (Ground Finch)	<i>fortis</i>
30	<i>Geospiza</i> (Ground Finch)	<i>fortis</i>
31	<i>Geospiza</i> (Ground Finch)	<i>fortis</i>
32	<i>Geospiza</i> (Ground Finch)	<i>fortis</i>
33	<i>Geospiza</i> (Ground Finch)	<i>fuliginosa</i>
34	<i>Geospiza</i> (Ground Finch)	<i>fuliginosa</i>
35	<i>Geospiza</i> (Ground Finch)	<i>fuliginosa</i>
36	<i>Geospiza</i> (Ground Finch)	<i>fuliginosa</i>
37	<i>Geospiza</i> (Ground Finch)	<i>fuliginosa</i>
38	<i>Geospiza</i> (Ground Finch)	<i>fuliginosa</i>
39	<i>Geospiza</i> (Ground Finch)	<i>magnirostris</i>
40	<i>Geospiza</i> (Ground Finch)	<i>magnirostris</i>
41	<i>Geospiza</i> (Ground Finch)	<i>magnirostris</i>
42	<i>Geospiza</i> (Ground Finch)	<i>magnirostris</i>
43	<i>Geospiza</i> (Ground Finch)	<i>magnirostris</i>
44	<i>Geospiza</i> (Ground Finch)	<i>scandens</i>
45	<i>Geospiza</i> (Ground Finch)	<i>scandens</i>
46	<i>Geospiza</i> (Ground Finch)	<i>septentrionalis</i>
47	<i>Geospiza</i> (Ground Finch)	<i>septentrionalis</i>
48	<i>Platypiza</i> (Vegetarian Finch)	<i>crassirostris</i>
49	<i>Platypiza</i> (Vegetarian Finch)	<i>crassirostris</i>
50	<i>Platypiza</i> (Vegetarian Finch)	<i>crassirostris</i>
51	<i>Platypiza</i> (Vegetarian Finch)	<i>crassirostris</i>
52	<i>Pinaroloxias</i> (Cocos Finch)	<i>inornata</i>
53	<i>Pinaroloxias</i> (Cocos Finch)	<i>inornata</i>

Table S1: The list of specimens of Darwin’s finches considered in our study.

Specimen ID	Genus	Species
54	<i>Coereba</i> (Bananaquit)	<i>flaveola</i>
55	<i>Coereba</i> (Bananaquit)	<i>flaveola</i>
56	<i>Coereba</i> (Bananaquit)	<i>flaveola</i>
57	<i>Coereba</i> (Bananaquit)	<i>flaveola</i>
58	<i>Coereba</i> (Bananaquit)	<i>flaveola</i>
59	<i>Euneornis</i> (Orangequit)	<i>campestris</i>
60	<i>Euneornis</i> (Orangequit)	<i>campestris</i>
61	<i>Euneornis</i> (Orangequit)	<i>campestris</i>
62	<i>Euneornis</i> (Orangequit)	<i>campestris</i>
63	<i>Euneornis</i> (Orangequit)	<i>campestris</i>
64	<i>Loxigilla</i> (Bullfinch)	<i>anoxanthus</i>
65	<i>Loxigilla</i> (Bullfinch)	<i>anoxanthus</i>
66	<i>Loxigilla</i> (Bullfinch)	<i>anoxanthus</i>
67	<i>Loxigilla</i> (Bullfinch)	<i>anoxanthus</i>
68	<i>Loxigilla</i> (Bullfinch)	<i>anoxanthus</i>
69	<i>Loxigilla</i> (Bullfinch)	<i>noctis</i>
70	<i>Loxigilla</i> (Bullfinch)	<i>noctis</i>
71	<i>Loxigilla</i> (Bullfinch)	<i>noctis</i>
72	<i>Loxigilla</i> (Bullfinch)	<i>noctis</i>
73	<i>Loxigilla</i> (Bullfinch)	<i>portoricensis</i>
74	<i>Loxigilla</i> (Bullfinch)	<i>portoricensis</i>
75	<i>Loxigilla</i> (Bullfinch)	<i>portoricensis</i>
76	<i>Loxigilla</i> (Bullfinch)	<i>portoricensis</i>
77	<i>Loxigilla</i> (Bullfinch)	<i>portoricensis</i>
78	<i>Loxigilla</i> (Bullfinch)	<i>violacea</i>
79	<i>Loxigilla</i> (Bullfinch)	<i>violacea</i>
80	<i>Loxigilla</i> (Bullfinch)	<i>violacea</i>
81	<i>Loxigilla</i> (Bullfinch)	<i>violacea</i>
82	<i>Loxigilla</i> (Bullfinch)	<i>violacea</i>
83	<i>Melopyrrha</i> (Cuban Bullfinch)	<i>nigra</i>
84	<i>Melopyrrha</i> (Cuban Bullfinch)	<i>nigra</i>
85	<i>Melopyrrha</i> (Cuban Bullfinch)	<i>nigra</i>
86	<i>Melopyrrha</i> (Cuban Bullfinch)	<i>nigra</i>
87	<i>Tiaris</i> (Grassquit)	<i>bicolor</i>
88	<i>Tiaris</i> (Grassquit)	<i>bicolor</i>
89	<i>Tiaris</i> (Grassquit)	<i>bicolor</i>
90	<i>Tiaris</i> (Grassquit)	<i>bicolor</i>
91	<i>Tiaris</i> (Grassquit)	<i>bicolor</i>
92	<i>Tiaris</i> (Grassquit)	<i>canora</i>
93	<i>Tiaris</i> (Grassquit)	<i>canora</i>
94	<i>Tiaris</i> (Grassquit)	<i>canora</i>
95	<i>Tiaris</i> (Grassquit)	<i>canora</i>
96	<i>Tiaris</i> (Grassquit)	<i>canora</i>
97	<i>Tiaris</i> (Grassquit)	<i>olivacea</i>
98	<i>Tiaris</i> (Grassquit)	<i>olivacea</i>
99	<i>Tiaris</i> (Grassquit)	<i>olivacea</i>
100	<i>Tiaris</i> (Grassquit)	<i>olivacea</i>

Table S2: The list of specimens of relatives of Darwin’s finches considered in our study.

	1/(Orbit curvature) of		
	Darwin's finches	DF relatives	All
Length x	0.711353	0.663881	0.722649
Width y	0.773172	0.816721	0.805499
Height z	0.760901	0.850506	0.819878

Table S3: Pearson correlation (Linear) between skull dimensions and 1/(orbit curvature).

	1/(Orbit curvature) of		
	Darwin's finches	DF relatives	All
Length x	0.739881	0.708161	0.758328
Width y	0.801726	0.842623	0.832067
Height z	0.774552	0.892692	0.844176

Table S4: Spearman correlation (Monotonic) between skull dimensions and 1/(orbit curvature).

	Orbit curvature of		
	Darwin's finches	DF relatives	All
Length x	-0.7359881	-0.681269	-0.744344
Width y	-0.801726	-0.812784	-0.797486
Height z	-0.774552	-0.864878	-0.828820

Table S5: Pearson correlation (Linear) between skull dimensions and the orbit curvature.

	Orbit curvature of		
	Darwin's finches	DF relatives	All
Length x	-0.642105	-0.708161	-0.758328
Width y	-0.744534	-0.842623	-0.832067
Height z	-0.710526	-0.892692	-0.844176

Table S6: Spearman correlation (Monotonic) between skull dimensions and the orbit curvature.

Variable	Length x	Width y	Height z	1/Curvature	Curvature
Ellipsoid semi-axis a	0.70	0.72	0.70	0.64	-0.67
Ellipsoid semi-axis b	0.80	0.87	0.83	0.62	-0.63
Ellipsoid semi-axis c	0.76	0.84	0.84	0.61	-0.62
1/Curvature	0.71	0.77	0.76	1.00	-0.98
Curvature	-0.74	-0.76	-0.75	-0.98	1.00

Table S7: Pearson correlation between various geometric quantities of Darwin's finches.

Variable	Length x	Width y	Height z	1/Curvature	Curvature
Ellipsoid semi-axis a	0.77	0.75	0.73	0.75	-0.75
Ellipsoid semi-axis b	0.88	0.96	0.89	0.81	-0.81
Ellipsoid semi-axis c	0.87	0.97	0.93	0.82	-0.82
1/Curvature	0.74	0.80	0.77	1.00	-1.00
Curvature	-0.74	-0.80	-0.77	-1.00	1.00

Table S8: Spearman correlation between various geometric quantities of Darwin's finches.

Variable	Length x	Width y	Height z	1/Curvature	Curvature
Ellipsoid semi-axis a	0.52	0.69	0.68	0.66	-0.62
Ellipsoid semi-axis b	0.76	0.95	0.94	0.85	-0.84
Ellipsoid semi-axis c	0.81	0.98	0.98	0.86	-0.87
1/Curvature	0.66	0.82	0.85	1.00	-0.97
Curvature	-0.68	-0.81	-0.86	-0.97	1.00

Table S9: Pearson correlation between various geometric quantities of the relatives of Darwin's finches.

Variable	Length x	Width y	Height z	1/Curvature	Curvature
Ellipsoid semi-axis a	0.76	0.87	0.84	0.79	-0.79
Ellipsoid semi-axis b	0.78	0.96	0.95	0.88	-0.88
Ellipsoid semi-axis c	0.80	0.95	0.96	0.90	-0.90
1/Curvature	0.71	0.84	0.89	1.00	-1.00
Curvature	-0.71	-0.84	-0.89	-1.00	1.00

Table S10: Spearman correlation between various geometric quantities of the relatives of Darwin's finches.

Variable	Length x	Width y	Height z	1/Curvature	Curvature
Ellipsoid semi-axis a	0.62	0.68	0.69	0.65	-0.66
Ellipsoid semi-axis b	0.81	0.92	0.89	0.74	-0.75
Ellipsoid semi-axis c	0.60	0.89	0.90	0.73	-0.75
1/Curvature	0.72	0.81	0.82	1.00	-0.97
Curvature	-0.74	-0.80	-0.83	-0.97	1.00

Table S11: Pearson correlation between various geometric quantities of both Darwin's finches and their relatives.

Variable	Length x	Width y	Height z	1/Curvature	Curvature
Ellipsoid semi-axis a	0.77	0.85	0.83	0.77	-0.77
Ellipsoid semi-axis b	0.84	0.97	0.95	0.84	-0.84
Ellipsoid semi-axis c	0.86	0.95	0.96	0.86	-0.86
1/Curvature	0.76	0.83	0.84	1.00	-1.00
Curvature	-0.76	-0.83	-0.84	-1.00	1.00

Table S12: Spearman correlation between various geometric quantities of both Darwin's finches and their relatives.